Transmission photometry of WASP-12b: simultaneous measurement of the planetary radius in three bands

C. M. Copperwheat,[1,2]⋆ P. J. Wheatley,[2] J. Southworth,[3] J. Bento,[4] T. R. Marsh,[2] V. S. Dhillon,[5] J. J. Fortney,[6] S. P. Littlefair[5] and R. Hickman[2]

[1]*Astrophysics Research Institute, Liverpool John Moores University, IC2, Liverpool Science Park, 146 Brownlow Hill, Liverpool L3 5RF, UK*
[2]*Department of Physics, University of Warwick, Coventry CV4 7AL, UK*
[3]*Astrophysics Group, Keele University, Keele, Staffordshire ST5 5BG, UK*
[4]*Department of Physics and Astronomy, Macquarie University, NSW 2109, Australia*
[5]*Department of Physics and Astronomy, University of Sheffield, Sheffield S3 7RH, UK*
[6]*Department of Astronomy and Astrophysics, University of California, Santa Cruz, CA 95064, USA*

ABSTRACT

Transmission spectroscopy has been successfully used from both the ground and in space to characterize the atmospheres of transiting exoplanets. This technique is challenging from the ground because ground-based spectrographs tend not to be designed to be photometrically stable, and effects such as variable slit losses cause significant systematic uncertainties. An alternative approach is to use simultaneous photometric observations in multiple wavebands to determine wavelength-dependent transit depth differences. We report an application of this technique to one of the hottest known exoplanets, WASP-12b, using the triple-beam camera ULTRACAM. We obtained simultaneous light curves in Sloan u', and two narrow-band filters centred on 4169 and 6010 Å, with full widths at half-maximum 52 and 118 Å, respectively. We fit these light curves with a photometric model and determine the planetary radius in the three different bands. Our data show no evidence for a difference in planetary radius over the wavelength range we study, and are consistent with an atmosphere that is dominated by Rayleigh scattering from a high-altitude haze, as well as more complicated atmosphere models which include the effects of molecules such as TiO. Our planetary radius measurements have an average precision of 2.6 per cent, compared to the ∼1.4–2.4 per cent radius differences predicted by the models over this wavelength range. We also find a consistent time of ingress and egress across our three wavebands, in contrast to the early ingress which has been reported for this system at shorter wavelengths.

Key words: planets and satellites: atmospheres – planets and satellites: individual: WASP-12b – stars: fundamental parameters – stars: individual: WASP-12 – planetary systems.

1 INTRODUCTION

The study of extrasolar planets (exoplanets) is one of the most rapidly advancing areas of modern astronomy. Around a third of known exoplanets have been observed to transit their host star, which provides a significant advantage for the elucidation of their nature, since not only does the edge-on viewing geometry remove the uncertainty in the inclination, but the light-curve shape itself is dependent on the sizes of the star and planetary components. The resulting mass–radius relation (e.g. Pollacco et al. 2008) provides the basis for understanding the structure, composition and evolution of the exoplanet population.

In addition to the mass–radius relation, transit observations provide the means to probe a variety of other physical properties of exoplanets. Observations over a range of wavelengths allow us to investigate the composition of the planetary atmospheres, since opacity sources raise the altitude of the photosphere at certain wavelengths and thus have a measurable effect on the planetary radius at those wavelengths. This *transmission spectroscopy* technique was applied to HD 209458b using the Space Telescope Imaging Spectrograph (STIS) on the *Hubble Space Telescope* (*HST*), resulting in the detection of atomic sodium in the planetary atmosphere (Charbonneau et al. 2002). Further STIS observations were obtained by Knutson et al. (2007), and a simultaneous fit of 10 photometric bandpasses yielded even more precise determinations of the planetary radius and orbital inclination. The discovery of atomic sodium in HD 209458b was followed by a number of detections of

⋆ E-mail: c.m.copperwheat@ljmu.ac.uk

other species in the upper atmosphere of exoplanets, using *HST* and the transmission spectroscopy technique (e.g. Vidal-Madjar et al. 2003, 2004; Lecavelier des Etangs et al. 2010). The atmosphere of HD 209458b has since been detected at low spectral resolution across the entire optical waveband, also using *HST* (Lecavelier des Etangs et al. 2008b; Sing et al. 2008). The resulting spectrum is dominated by a blue broad-band opacity source, interpreted as Rayleigh scattering by H_2, as well as a Stark-broadened component of the Na I line. A low-resolution *HST* spectrum of HD 189733b also showed an atmospheric haze, in this case a scattering continuum from a haze of submicrometre particles (Pont et al. 2008; Sing et al. 2011).

There have been a number of successful applications of the technique of transmission spectroscopy from the ground. This has resulted in the confirmation of sodium absorption (Redfield et al. 2008; Snellen et al. 2008), and the detection of Hα (Jensen et al. 2012) in the atmospheres of both HD 189733b and HD 209458b. Other recent examples are the detection of sodium in WASP-17b (Zhou & Bayliss 2012) and sodium and potassium in XO-2b (Sing et al. 2012). However, transmission spectroscopy has been more challenging from the ground because ground-based spectrographs tend not to be designed to be photometrically stable, and effects such as variable slit losses cause significant systematic uncertainties. The best precision is currently achieved using multi-object spectrographs (e.g. Bean, Miller-Ricci Kempton & Homeier 2010). Simultaneous observations of the target and multiple comparison stars allow atmospheric variations to be accounted for, and wide entrance apertures minimize slit losses.

An alternative approach from the ground is to take simultaneous photometric observations in multiple bands, and then fit the transit light curve in each band in order to detect differences in the planetary radius with wavelength. This avoids some of the complications associated with spectroscopy, at the price of spectral resolution. However, since observations have shown many planetary atmospheres are dominated by broad-band features, photometric observations can still be an effective means of distinguishing between models. A recent example of this technique was presented in Southworth et al. (2012a), with simultaneous observations in Strömgren *u*, Gunn *g* and *r* and Johnson *I* filters of a transit in the HAT-P-5 system. They found the planetary radius to be larger in *u*, but could not rule out systematic errors as the cause of this difference.

In 2009 we obtained a transit of WASP-12b with the triple-beam high-speed CCD camera ULTRACAM (Dhillon et al. 2007) mounted on the 4.2-m William Herschel Telescope (WHT). WASP-12b was discovered by the SuperWASP collaboration (Hebb et al. 2009), and at the time of its discovery (and our follow-up observations) it was the hottest transiting exoplanet known, making it an excellent target with which to test atmosphere models. In addition, recent *HST* Cosmic Origins Spectrograph (COS) observations of this star were interpreted by Fossati et al. (2010) to show an early ingress of the exoplanet at near-ultraviolet (UV) wavelengths. This has been modelled as due to the Roche lobe overflow of material from the star (Lai, Helling & van den Heuvel 2010) or alternatively due to a bow shock of coronal material around the magnetosphere of the planet (Llama et al. 2011). Simultaneous observations in multiple optical wavebands provide a test of these models.

2 OBSERVATIONS AND REDUCTION

On the night of 2009 January 4 we observed WASP-12b for 10 h, beginning at 19:34 UT and covering one transit, using the fast photometer ULTRACAM mounted on the WHT. ULTRACAM is a

triple beam camera, taking observations simultaneously in three bands. Typically it is used with Sloan broad-band filters, but we chose to use narrow-band filters in the green and red arms in order to minimize atmospheric trends, as we will discuss in Section 3.1. In the green arm we used a filter with a central wavelength of 4169 Å and a full width at half-maximum (FWHM) of 52 Å. In the red arm we used a filter with a central wavelength of 6010 Å and a FWHM of 118 Å. We retained the Sloan *u'*-band filter in the blue arm (central wavelength 3557 Å, FWHM 599 Å). An additional motivation for this choice of filters was the theoretical work of Fortney et al. (2008), which presented two classes of model atmospheres, one of which features appreciable opacity at certain wavelengths due to TiO and VO. In order to try and detect this effect we chose narrow-band filters in which the disparity between the observed planetary radii is predicted to be at its greatest (as shown in fig. 11 of Fortney et al. 2008).

For the majority of the observation we used a 5.8 s exposure time. The images were unbinned, and the full frame of the CCD was used with the fast readout mode. The dead time between exposures for ULTRACAM is ∼25 ms. The night was photometric with acceptable (∼1 arcsec on average) seeing, although the seeing was quite variable on short time-scales, particularly in the early part of the night. As has become fairly standard in observations of planetary transits we applied a modest defocus of the telescope such that the FWHM was ∼2 arcsec. Aside from the possibility of saturation when observing a bright star like WASP-12 ($B = 12.1$), the purpose of the defocus is to reduce the systematic uncertainty introduced by the flat-fielding, since by increasing the FWHM, the contribution of any one individual pixel to the overall measured flux is reduced. This uncertainty is potentially quite important, and for the same reason the star should ideally be held in the same position on the chip over the course of the observation. We relied on the autoguider and did see a drift in pixel position over the course of our observation of 10–15 pixels (3–4.5 arcsec), but we find no evidence that this drift introduces any systematic trend into our data.

These data were reduced with aperture photometry using the ULTRACAM pipeline software,[1] with debiassing, flat-fielding and sky background subtraction performed in the standard way. Flat-fielding was performed using ∼500 sky flats which were obtained on the same night as the transit observation. The source flux was determined using a variable aperture, whereby the radius of the aperture is scaled according to the FWHM. The scaling factor for each band was determined empirically by reducing each data set with a range of possible factors, and choosing the ones which produced the light curves with the lowest scatter in a small section of the out-of-transit data. The use of a variable aperture can potentially cause problems when applied to defocused observations, due to the reduction routine failing to determine correct centroid and FWHM values. However, in a case such as this where we have only applied a small defocus we found the variable aperture method to be somewhat superior to using a fixed aperture by comparing the signal-to-noise ratio (S/N) obtained in each case. The centroiding was performed using a Moffat profile fit. As well as the target we also selected and reduced seven comparison stars (listed in Table 1) which we used to correct short-time-scale transparency variations in our target light curves, as well as the longer time-scale atmospheric trends. This process is described in detail in Section 3.1. The positions of these comparison apertures were fixed relative to

---

[1] http://deneb.astro.warwick.ac.uk/phsaap/software/ultracam/html/index.html

Table 1. Coordinates of the comparison stars we used for the differential photometry.

#	Name	RA ($^{h}:^{m}:^{s}$)	Dec. ($^{\circ}:':''$)
1	TYC 1891-326-1	06: 30: 39.8	+29: 37: 40.4
2	TYC 1891-324-1	06: 30: 48.3	+29: 39: 35.9
3	TYC 1891-38-1	06: 30: 49.9	+29: 38: 54.7
4		06: 30: 46.40	+29: 41: 12.8
5		06: 30: 45.81	+29: 41: 28.0
6		06: 30: 32.23	+29: 37: 34.7
7		06: 30: 43.23	+29: 37: 53.7

the position of the primary aperture, which helps the centroiding for these fainter stars. Where appropriate we used the ULTRACAM software to mask fainter stars which overlap with the sky apertures. 'Lucky Imaging' observations have detected a faint M-dwarf star approximately 1 arcsec from WASP-12b (Bergfors et al. 2013). This is too close to the target to mask, but likely contributed a negligible amount of flux at the wavelength range we study. For all data we convert the MJD times to the barycentric dynamical time-scale (TDB), correcting for light travel times. We did not use the section of data obtained at the very end of the night at high (>2) airmasses, as we found no benefit to the parameter determinations when we included these data.

3 LIGHT CURVES AND MODEL FITTING

3.1 Atmospheric effects

In differential photometry both the target star and a nearby, photometrically stable comparison star are reduced simultaneously using the same sized apertures. The light curve of the target is then divided by the light curve of the comparison. If the comparison is close enough to the target this should remove the short (~exposure time) time-scale variation due to changes in transparency. It should also remove any long time-scale trends in the data. The most significant of these is the variation in the target and comparison count rate due to the changing airmass. The response of the star to changing airmass varies with colour, and so to optimize this correction the comparison star is required to be very close in colour to the target. In the WASP-12b field, we found the brighter comparison stars are not a sufficiently good colour match to remove the airmass trend at the level of photometric precision required (~1 per cent), and so when we divided through by the comparison star there were residual trends. We attempted to minimize this effect by using narrow-band filters in the red and green arms. If the filter is narrow enough such that the stellar spectrum is essentially flat over the wavelength range sampled, then the colour difference between the target and comparison will not matter and the light curve should be flattened via the differential photometry without resorting to any further manipulation. This choice came at the price of a reduced count rate in these arms, and in practice we found there was still a residual slope in the differential light curve, albeit much smaller than we find in the blue arm (in which we retained the broad-band u' filter). There may be other contributing factors to the long-term trends, for example we considered the effect of telescope vignetting: if the two stars are at different positions on the CCD from the rotation axis of the telescope, then as the observation proceeds the rotation of the field may result in an appreciable trend. This is distinct from the instrumental vignetting, which should not change over the course of the observation as long as the star is maintained in the same position on the CCD. However, the fact that the use of narrow-band filters

offers a significant improvement implies that the colour difference between the target and comparison star is the dominant factor.

We found that the combination of multiple companion stars provided a superior correction of the atmospheric trends compared to using a single star. Accordingly, we selected the seven stars listed in Table 1. These are stars which we found to be photometrically stable, which were bright in all three arms and did not coincide with hot pixels or bad columns on the ULTRACAM CCDs. Ideally we would use a comparison star which is brighter than the target, but unfortunately WASP-12 is the brightest star in the field of view, although comparisons 1 and 2 are close in brightness in the green and red arms. We averaged these seven stars together and divided the target light curves by this average. The price of this superior correction for the atmospheric trends was a reduced S/N. The trend was not removed completely – potentially further improvement could be found by including even more comparison stars, but the remaining stars in the field of view are significantly fainter, and so the subsequent reduction in S/N is too great. We preferred to fit this residual trend as a component in our model, and discuss this in more detail in Section 3.2 along with the other model components.

In many analyses of exoplanet light curves obtained from the ground, the light curves are flattened with a polynomial which has been fitted to the out-of-transit data, before performing the model fit through which the physical parameters are determined (e.g. Southworth et al. 2009). The problem with this is that it is often unclear if uncertainty introduced by the initial fit is reflected in the final parameter determinations. Choice of polynomial can also dramatically affect the transit depth, and the sections of out-of-transit data used for the polynomial are often quite small, even if a complete night is spent on target. A polynomial correction outside of the main model fit is particularly unwise in a case such as this in which we are comparing transit depths in different light curves. Potentially some of the inconsistencies in transit depth determinations which can be found in the literature are due to this practice.

We also considered more complicated approaches to the problem of atmospheric correction. Instead of making an unweighted average of comparison stars, or an average weighted by luminosity, one approach is to have the weights as free parameters and fit them so as to minimize the out-of-transit trends. Another approach is, rather than dividing by the average of the comparisons stars, to instead fit a high order (10+) polynomial to each comparison light curve. The average of these polynomials is then used to remove the long-term variation from the brightest comparison, and the target light curve is then divided by the corrected light curve of this single comparison to remove the short-term variation. This method should correct the trends in the same way but without any reduction to the S/N. We tried this approach, but found that when we fitted these light curves with our model the uncertainties on the resultant parameter determinations showed no significant improvement, implying it is systematic factors rather than the photon noise which dominates. We chose therefore for clarity to use the simpler method of averaging the comparison stars, as described above.

3.2 The light-curve model

We modelled the planetary transit using the LCURVE light-curve fitting code written by T. Marsh, which is described in detail in the appendix of Copperwheat et al. (2010). This code was originally designed to model the light curves of eclipsing cataclysmic variables. We used a modified version of this code in which the accretion disc and bright spot components are removed, and the secondary component has a spherical rather than Roche lobe filling geometry.

Modified in this way the LCURVE code can be used to describe a detached eclipsing binary or, by setting the flux contribution from the secondary to zero, a transiting exoplanet. The parameters of the model in this case are the mass ratio q and the inclination i, the radii of the star and the planet R_* and R_{pl}, which we express in terms of the orbital separation a, the time of mid-transit t_0, the orbital period P and the stellar limb darkening coefficients. We also accounted for the residual airmass trend in our data by multiplying the model by

$$1 + t(A + Bt), \tag{1}$$

where t is the time scaled such that it varies from -1 to 1 from the beginning to the end of the data, and A and B are additional parameters in the fit.

3.3 The limb darkening coefficients

Our parameter of interest is the planetary radius, R_{pl}, which is determined by the depth of the transit. The stellar limb darkening is correlated with this parameter, and so both our choice of limb darkening law and our choice of starting values are important. Southworth (2008) discussed the various limb darkening laws as applied to exoplanet transits in detail. He emphasized the importance of using a non-linear law but noted that using a law with more than two coefficients offered no significant improvement using ground-based data of contemporary quality. Given the importance of this model component, we chose to fit the data twice using two different laws: the polynomial (quadratic) law,

$$\frac{I(\mu)}{I(1)} = 1 - u_{1*}(1 - \mu) - u_{2*}(1 - \mu)^2, \tag{2}$$

and the two-coefficient form of the non-linear law first presented in Claret (2000),

$$\frac{I(\mu)}{I(1)} = 1 - u_{1*}(1 - \mu^{1/2}) - u_{2*}(1 - \mu). \tag{3}$$

In these equations u_{1*} and u_{2*} are the two limb darkening coefficients, $I(1)$ is the specific intensity at the centre of the disc and μ is defined by $\cos(\gamma)$, where γ is the angle between the line of sight and the emergent intensity.

For both laws the two limb darkening coefficients are correlated with each other. Following Southworth (2008) we fix u_{1*} in the three bands to values which are physically appropriate for the star, and fit u_{2*}. For the starting values we use the tables in Claret & Bloemen (2011), interpolating to find coefficients appropriate for a star with the correct $\log g$ and T_{eff} (using the values for WASP-12 given in Hebb et al. 2009). There are no tables available for the narrow-band filters we use, so we assume the Sloan g and r tables are approximately correct for our green and red narrow-band filters. We also assume a solar metallicity and a zero microturbulent velocity for the star. While these various assumptions may not be correct, they are sufficient to provide a physically appropriate starting point for our fits.

3.4 The model fit

For the model fitting, we used a Markov chain Monte Carlo (MCMC) method. This method, properly applied, potentially explores the parameter space more extensively than alternative minimization techniques, and gives us confidence that we are finding the true minima. Our MCMC technique was described in the appendix of Copperwheat et al. (2010). As in that work we used multiple MCMC chains of $10\,000+$ jumps to ensure that we

obtained consistent results, although with this simplified version of the light-curve model we tend to find convergence with a much smaller number of jumps. We ran two separate series of chains, using the quadratic limb darkening law for the star in one, and the non-linear Claret law in the other. q is not constrained by our data and must be fixed – we used the value determined by Hebb et al. (2009). Similarly, with only a single transit of data allowing P to vary has no effect on our parameter determinations, so we fix this to the literature value. Additionally, there is a degeneracy between R_* and i which can cause a problem when these parameters are fitted simultaneously, since they are both correlated with the transit duration. We therefore use a Gaussian prior to enforce a value for i close to the Hebb et al. (2009) value, with a standard deviation equal to the 1σ error. We use flat, non-informative priors for the other parameters in the model fit. The complete list of parameters that we fitted is i, R_*, R_{pl}, t_0, A, B and the limb darkening coefficient u_{2*}.

One enhancement we made here to the method described in Copperwheat et al. (2010) was to fit the three bands simultaneously. This was a relatively simple modification in which the χ^2 value governing the jump probability was determined from the combination of the values in the three individual bands. This modification enabled us to establish common parameters which were fit simultaneously in the three bands. We therefore determine a single, common value for t_0, R_* and i, the parameters which are not wavelength dependent. We list our final parameter determinations in Table 2. These values are the means and standard deviations from the posterior distributions. The light-curves and best-fitting models are plotted in Fig. 1.

4 RESULTS

As is apparent in Fig. 1 the model fit to the light curves is acceptable. We find a χ^2_{red} of ~ 1.2 (293 N_{dof}) in the green arm (4169 Å) and ~ 1.5 in the other two arms. We do not find a significant difference in the quality of fit when we change limb darkening laws. The residuals show some variation, some of which might be intrinsic, but is more likely due mainly to atmospheric transmission and instrumental effects such as the flat-field 'noise' which can be apparent in photometric studies at this level of precision (see e.g. Southworth et al. 2009 for a discussion of this). Our MCMC fitting method assumes the uncertainty on each data point is Gaussian distributed and independent of all other points, so any correlated noise component ('red noise') will impact the reliability of our quoted uncertainties. Our residuals do not show any strong evidence for such a correlated component. In particular, we note that there are no apparent long-term trends in the residuals, and the model seems to fit the transit data (and the ingress/egress features) just as well as the out-of-transit data. The absence of any trends in the residual is significant: as we discussed earlier the target light curves were not flattened before fitting other than by dividing through by the average of the comparison light curves. It is clear in the data (particularly the blue arm, broad-band data) that some long-term trends remain in the light curves. The fact that we do not see this trend in the residuals demonstrates that the polynomial component of our model provides an adequate fit.

Our parameter determinations are consistent with the values reported by Hebb et al. (2009). In the case of the inclination this was enforced due to the Bayesian prior constraint in our model fitting. For the planetary radius, Hebb et al. (2009) find $1.79 \pm 0.09 R_J$ using B- and z-band photometry. Our determinations tend to be a little larger than this value but are consistent with it (e.g. $1.93 \pm 0.05 R_J$

Table 2. Results from our MCMC fits. The parameters are the mass ratio q, the orbital inclination i, the stellar (R_*) and planetary ($R_{\rm pl}$) radii scaled by the orbital separation a, the time of mid-transit t_0, the orbital period P, the first and second stellar limb darkening coefficients u_{1*} and u_{2*} and the two coefficients for the airmass trend A and B. We list separately results obtained using a polynomial limb darkening law and the Claret (Claret & Bloemen 2011) law. The values of q and P were fixed to the values given in Hebb et al. (2009). i, R_*/a and t_0 were varied in the fit but held to the same value in all three bands.

Parameter	SDSS u'	4169 Å	6010 Å
		Polynomial limb darkening law	
q		0.000996	
i (°)		82.52 ± 1.04	
R_*/a		0.3362 ± 0.0057	
$R_{\rm pl}/a$	0.03933 ± 0.00105	0.04033 ± 0.00108	0.03970 ± 0.00094
t_0 (d)		54835.90326(13)	
P (d)		1.091423	
u_{1*}	0.5615	0.4647	0.3141
u_{2*}	0.399 ± 0.061	0.487 ± 0.075	0.339 ± 0.063
A	0.00413 ± 0.00016	-0.00177 ± 0.00019	-0.00128 ± 0.00009
B	-0.00241 ± 0.00023	0.00253 ± 0.00029	0.00185 ± 0.00014
		Claret limb darkening law	
q		0.000996	
i (°)		83.32 ± 1.30	
R_*/a		0.3302 ± 0.0064	
$R_{\rm pl}/a$	0.03852 ± 0.00119	0.03960 ± 0.00114	0.03906 ± 0.00097
t_0 (d)		54835.90327(13)	
P (d)		1.091423	
u_{1*}	0.1632	0.2272	0.3326
u_{2*}	0.719 ± 0.032	0.626 ± 0.041	0.300 ± 0.029
A	0.00416 ± 0.00015	-0.00173 ± 0.00020	-0.00125 ± 0.00009
B	-0.00240 ± 0.00024	0.00251 ± 0.00030	0.00186 ± 0.00014

and $1.90 \pm 0.05R_{\rm J}$ for the two green arm fits, using the equatorial Jupiter radius of 71 492 km). The Hebb et al. (2009) determination made WASP-12b the fifth largest exoplanet currently known, but our new measurement places it in competition with WASP-17b ($1.93 \pm 0.05R_{\rm J}$; Southworth et al. 2012b) for first place. Our measurement of t_0 shows no evidence of a transit time variation when compared to the Hebb et al. (2009) ephemeris. Recently Maciejewski et al. (2013) reported a variation which they attributed to a second planet on a 3.6 d eccentric orbit. Using their ephemeris our data are still consistent with no variation, however, the epoch of our observation is close to a phase of 0 for the sinusoidal timing variation they detect, and so our data are also consistent with the presence of this second planet.

In Figs 2 and 3 we plot the distributions of the results from the MCMC runs for the green arm (4169 Å) data, for the two different stellar limb darkening laws. We do not plot the results for the red and blue arms, but they show similar distributions. We vary seven parameters in our model fits. The key parameter is the planetary radius, so we plot this parameter against the other six in order to explore our confidence in these radius determinations.

We begin by discussing the limb darkening. We fitted our data twice, using a polynomial limb darkening law and also the Claret law. The results listed in Table 2 show that these two models provide consistent results, although using the polynomial law leads to a slightly higher planetary radius determination. The value of the limb darkening coefficient u_{2*} of course differs depending on which law is used. The fact that the two laws provide consistent results is important because we see in the distributions that u_{2*} can be somewhat correlated with the planetary radius, and so the fact

that choice of law does not significantly bias our results increases confidence in our findings. As discussed in Section 3.3 we chose to fix u_{1*} and vary u_{2*}, since these two parameters are degenerate in our model. We explored the effect of perturbing our u_{1*} values from our original estimates and refitting the data, and we found that this does not have a significant effect on our results with the exception of our u_{2*} determination, which changes to compensate for any change in u_{1*}.

We also investigated how our fitted limb darkening coefficients compare to stellar model atmosphere predictions. For this we used the Kurucz (1979) models.[2] We interpolated between the published grids to obtain models with a temperature and log g appropriate for WASP-12, and convolved these grids with our filter response functions to obtain $I(\mu)/I(1)$ for each filter. We then used a least-squares method to obtain the optimum values of u_{2*} for each filter and limb darkening law. As in the fits to our data, we fixed u_{1*} to the values listed in Table 2. In general, the limb darkening coefficients predicted from these model atmosphere calculations are in reasonable agreement with the results of our model fits. When the polynomial law is used we predict values of 0.295, 0.401 and 0.364 in the blue, green and red arms, respectively. The blue arm prediction is 1.8σ smaller than our fitted value, but the values for the other two arms are $\sim 1\sigma$ or less from the fitted values. For the Claret law the predictions for u_{2*} from the model atmospheres are 0.697, 0.648 and 0.374. In this case the red arm prediction is 2.5σ greater than the

[2] http://kurucz.harvard.edu/
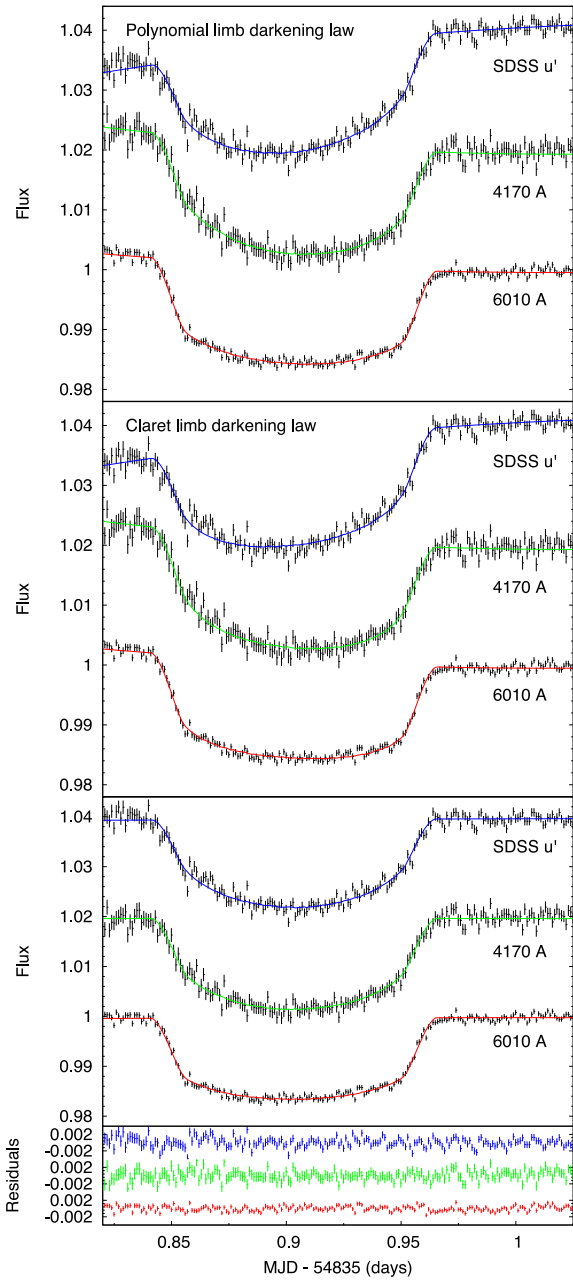
Figure 1. Light curves of WASP-12, after dividing by the averaged light curves of the comparison stars, as described in Section 3.1. The data plotted here are binned such that the time between data points is ∼85 s. The solid lines show the results of our model fits. In each panel we plot from top-to bottom the blue arm (SDSS u'), green arm (4169 Å) and red arm (6010 Å) data and models, with offsets of 0.02 and 0.04 for the green and blue arms. Top panel: model fit when the polynomial limb darkening law is used for the star. Second panel: model fit when the Claret law is used for the star. Third panel: aside from the use of comparison stars to obtain differential photometry, no other correction has been applied to flatten the light curves plotted in the first two panels. Some long-term trend remains (probably mostly airmass related), which we fit as a component in our model. Here we plot the polynomial data and model again, but with this component subtracted. Bottom panel: residuals from the polynomial model. The Claret model residuals are very similar.

determination from our fits, but the other two predictions are very close to our results.

Turning to the stellar radius and the inclination, we see in Figs 2 and 3 that these two parameters show a strong correlation with the planetary radius. They are also strongly correlated with each other, which was why we considered it necessary to use a Bayesian prior to enforce a value for the inclination close to the Hebb et al. (2009) value. These parameters could have been fixed in our fits but this would result in an underestimation of the uncertainties in our planetary radius determinations. We also experimented with fixing one or the other of these parameters to the literature value, and leaving the other as a free parameter. This resulted in a determination for the free parameter which was as much as 2σ different to the literature value, with a corresponding difference in the determination of the planetary radius. However, the difference in the planetary radius determination was about the same for each light curve, with very little relative difference between the determinations in the three wavebands. This is undoubtedly due to the fact that we fit the three simultaneously. This demonstrates the power of a multibeam camera for a study of this nature. Our conclusion is that while these parameters might introduce a systematic bias into our radius determinations, it should not affect the relative measurements and hence the conclusions we draw in Section 5.1.

Of the remaining three parameters, we see that there is no obvious correlation between planetary radius and the time of mid-transit (t_0) or the quadratic term B in the airmass trend. Possibly in the polynomial law case there might be a weak correlation between the radius and the linear term A, which highlights the importance of including these trends as a component in the model fit so they can be properly characterized using the complete data set.

5 DISCUSSION

5.1 Planetary radius and wavelength

In Fig. 4 we plot our determination of the planetary radii with wavelength. As well as a radius scale in units of orbital separation a, we also indicate the range in terms of atmospheric scale heights, which we calculate by assuming a Jupiter composition for the planet, and the temperature and $\log g$ from Hebb et al. (2009). We plot results for the two limb darkening laws separately. The two laws provide consistent results, and we see no significant difference in planet radius with wavelength.

HST transmission spectroscopy of HD 209458b (Lecavelier des Etangs et al. 2008b; Sing et al. 2008) and HD 189733b (Pont et al. 2008; Sing et al. 2011) shows their spectra to be dominated by a broad-band opacity source interpreted as scattering by an atmospheric haze. We calculated the predicted effect of Rayleigh scattering for WASP-12b over the wavelength range of our filters. Lecavelier des Etangs et al. (2008a) determined the effective transit measured altitude of a hydrostatic atmosphere as a function of wavelength. Then, by assuming a scaling law for the absorption cross-section of the form $\sigma = \sigma_0 (\lambda/\lambda_0)^\alpha$, the slope of the planetary radius as a function of wavelength is given by

$$\frac{\mathrm{d}R_{\mathrm{pl}}}{\mathrm{d}\ln \lambda} = \alpha H, \tag{4}$$

where H is the atmospheric scale height. Following Lecavelier des Etangs et al. (2008a), to model Rayleigh scattering we set $\alpha = -4$. We plot the resulting slope as a red (solid) line on Fig. 4. The dashed lines show the uncertainty in the slope, which is due to the uncertainty in the scale height determination. We apply an arbitrary
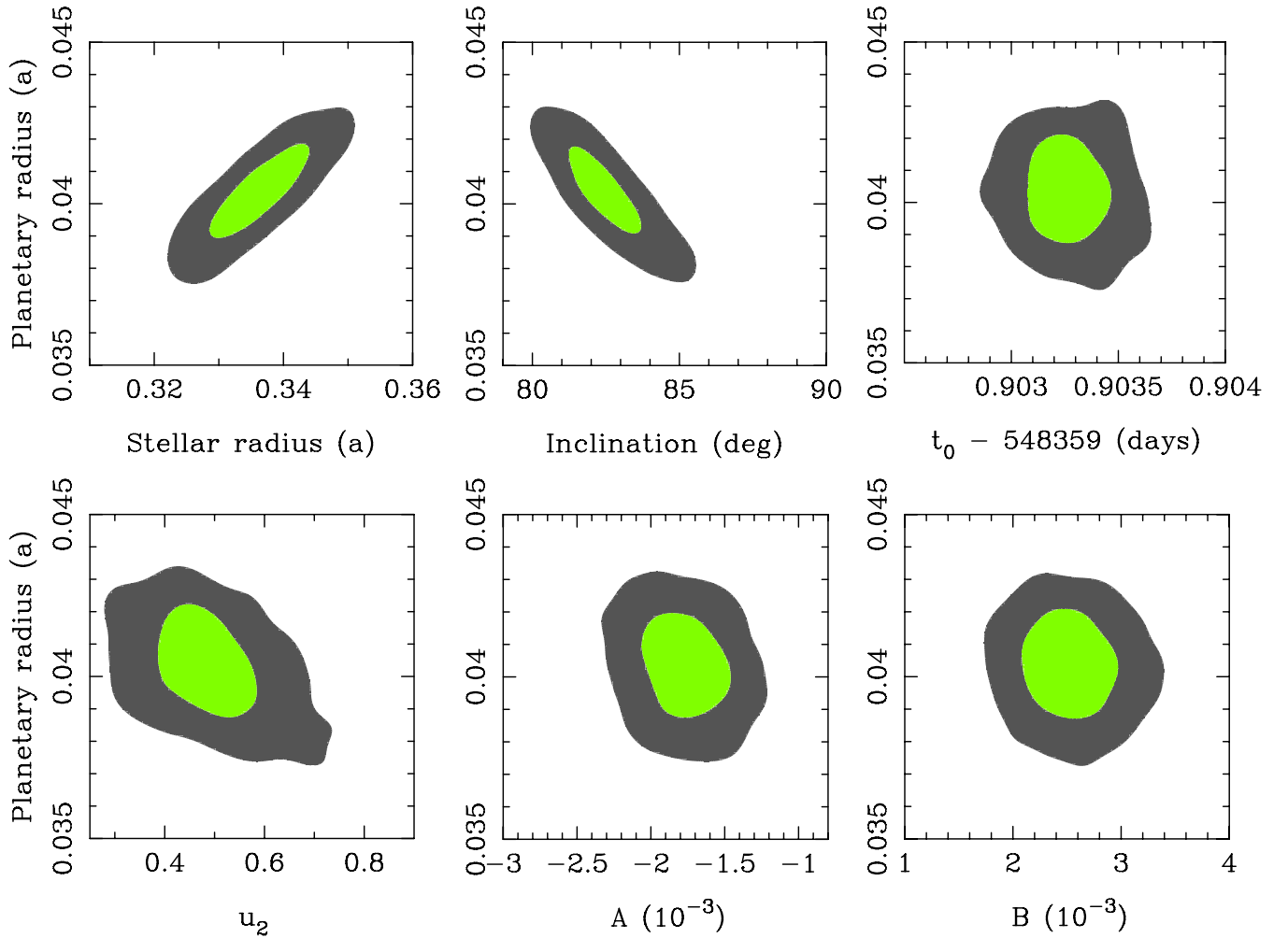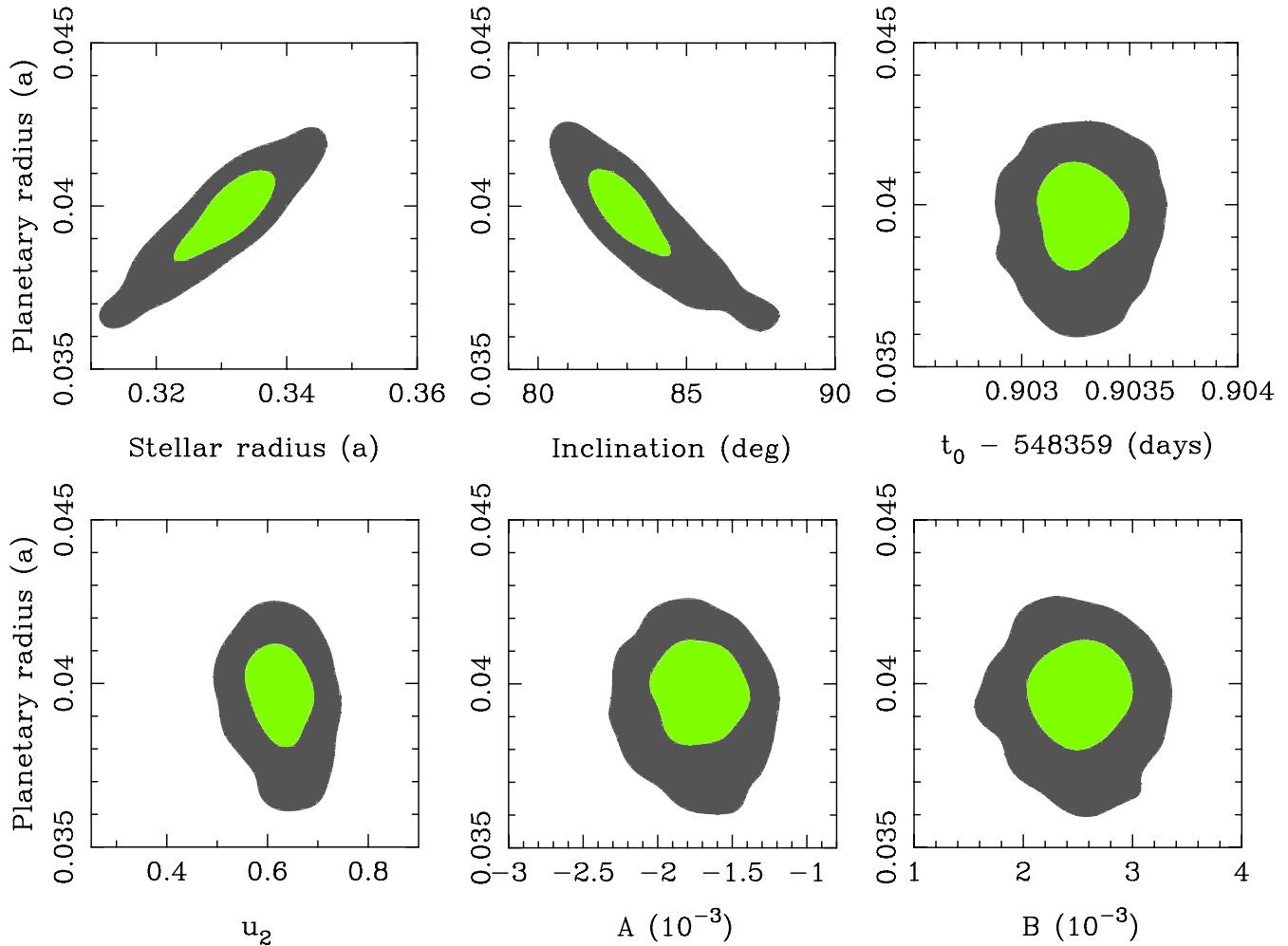
Figure 2. The distribution of the results from the MCMC runs for the green arm (4169 Å) data when the polynomial limb darkening law is used for the star. The red and blue arm results follow similar distributions. We plot the planetary radius R_{pl}/a against the other six parameters which are allowed to vary in our model fits. The green and grey regions indicate the 1σ and 3σ confidence intervals, respectively.

offset to make the best fit of the Rayleigh scattering lines match to our radius determinations. We find that over the wavelength range we study the expected difference in planetary radius for this atmospheric model is only around 3–4 scale heights. Hence Rayleigh scattering from a high-altitude haze is consistent with our findings. Scattering via a haze of submicrometre particles, in which α would be closer to zero, is equally consistent.

Other atmospheric opacity sources have been predicted, but not yet observed. Planetary atmospheres in emission have been detected with *Spitzer* (e.g. Deming et al. 2005), revealing a wide range of brightness temperatures compared with expected equilibrium temperatures (Harrington et al. 2007). These *Spitzer* results were interpreted by Fortney et al. (2008) as resulting from two distinct classes of exoplanet atmosphere. The optical opacity of the hottest exoplanets (termed 'pM class' planets) was predicted by their model to have atmospheres which are dominated by TiO and VO absorption bands, whereas in cooler planets ('pL-class') the TiO should have condensed out of the atmospheres and the dominant opacity sources are Na and K. We computed both models for WASP-12b, using the code described in Fortney et al. (2010). For the stellar and planetary parameters we use the Hebb et al. (2009) values with the exception of the radii, for which we used our own determinations.

The two models are plotted in Fig. 4, with the green (dashed) line showing the hotter, TiO/VO-dominated model, and the blue (dot–dashed) line showing the cooler, Na/K-dominated model. Given the temperature of WASP-12b (estimated as 2516 ± 36 K by Hebb et al. 2009) we would expect the hotter model to provide a better fit to our data, however, we find that both models are consistent with our radius measurements to within the uncertainties. For this planet these atmosphere models remain a viable alternative to the simple Rayleigh scattering case.

Recently Stevenson et al. (2013) presented multi-object transmission spectroscopy of WASP-12b over the wavelength range $\sim$0.7–1 μm obtained with the Gemini Multi-Object Spectrograph (GMOS) instrument mounted on the Gemini-North telescope. They find these data rule out a cloud-free H_2 atmosphere with no additional opacity sources. They also reanalysed *HST/*Wide Field Camera 3 (WFC3) near-infrared and *Spitzer Space Telescope* data (originally published in Swain et al. 2013 and Cowan et al. 2012, respectively) to obtain a combined transmission spectrum over the wavelength range 0.7–5 μm. There is evidence for a number of broad features in this spectrum, but the data are consistent with both O-rich and C-rich models, making them difficult to identify. Our data lie bluewards of all of these observations and so extends

Figure 3. Green arm (4169 Å) MCMC distributions when the Claret limb darkening law is used for the star. The red and blue arm results follow similar distributions. We plot the planetary radius R_{pl}/a against the other six parameters which are allowed to vary in our model fits. The green and red regions indicate the 1σ and 3σ confidence intervals, respectively.
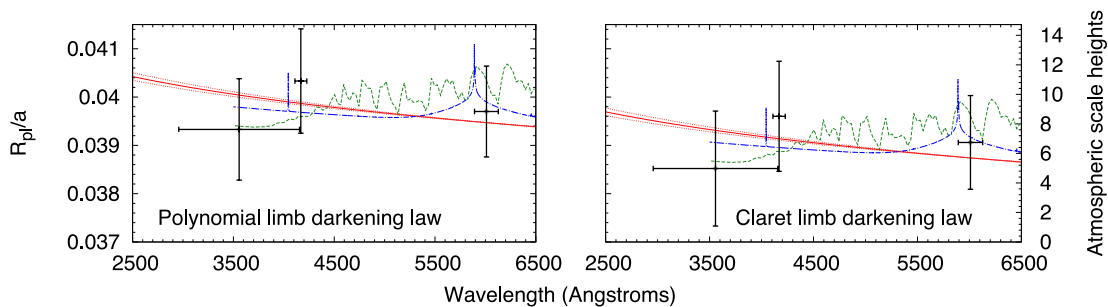
Figure 4. The planetary radius scaled by the orbital separation a in each filter, as determined from our MCMC fit. We mark each measurement at the central wavelength of the filter used, with the uncertainty set to the FWHM of the filter. The right-hand axes are labelled in units of atmospheric scale heights, determined by assuming a Jupiter composition and the temperature and $\log g$ from Hebb et al. (2009). The red (solid) lines running across the plot show the predicted change in planetary radius with wavelength assuming Rayleigh scattering from a high-altitude haze. This calculation also uses the scale height, and the dotted lines show the uncertainty in this determination. The other lines show model planetary atmospheres calculated using the method described in Fortney et al. (2010). The green (dashed) line is for a 'pM-class' atmosphere in which the opacity is dominated at this wavelength range by TiO and VO, whereas the blue (dot–dashed) line is for a 'pL-class' atmosphere in which the dominant opacity sources are Na and K. An offset is applied to all three models to provide the best fit to our radius measurements.

the wavelength range of the spectrum, however, in order to combine data sets it is necessary to use the same orbital parameters. We therefore ran our MCMC fits again, but this time using the inclination and stellar radius from Stevenson et al. (2013) as Gaussian priors. Stevenson et al. (2013) present their findings in terms of the transit depth $(R_{pl}/R_*)^2$. In our new fits we measure the transit depth to be 1.42 ± 0.03, 1.46 ± 0.04 and 1.43 ± 0.03 per cent in the blue, green and red arms, respectively. Fig. 19 of Stevenson et al. (2013)

shows that these values are similar to the transit depths measured in the GMOS data between 0.7 and 1 μm, implying that the planetary spectrum is fairly flat from this point down to ~0.3 μm.

5.2 No evidence for an early ingress in the blue arm

Fossati et al. (2010) presented near-UV (2539–2811 Å) *HST* transmission spectra of WASP-12b. They claimed that these data showed an early ingress of the exoplanet at these wavelengths, which they speculated was due to a disc of previously stripped material. These data were recently re-analysed in Haswell et al. (2012), and the same conclusion was reached: table 4 of that paper reports an average phase offset of ~− 0.034 (~0.037 d) when the near-UV measurements are compared to the optical transit. Some authors have suggested that an early ingress could be due to a highly irradiated exoplanet overflowing its Roche lobe, leading to outflows of material from the Lagrangian points (Lai et al. 2010; Bisikalo et al. 2012). Alternatively, an early ingress could be caused by a bow shock of coronal material around the magnetosphere of the planet (Llama et al. 2011).

Simultaneous transit observations in multiple optical wavebands provide a test of this result. The u'-band filter we use is redwards of the near-UV data presented by Fossati et al. (2010), but since this filter covers the Balmer jump region then it is likely that we would detect in this filter the same absorbing material that is postulated to cause the effect at near-UV wavelengths. However, we see in Fig. 1 that there is no difference in the ingress time in our three wavebands. An offset of the order of 0.037 d would be clearly detectable, and since we fitted the three light curves with the same time of mid-transit t_0, the fit in the u' band would be significantly poorer if this offset were present. Additionally, the early ingress models all imply an asymmetry between the ingress and egress features. We do not observe this: our model cannot account for such an asymmetry so this would also manifest itself as a poor fit around these features. As an additional check we fitted the u'-band data again, separately from the other two wavebands. We find the subsequent parameter determinations are consistent with the findings from the simultaneous fit. We conclude that there is no evidence for an early ingress over this wavelength range.

6 CONCLUSIONS

In this paper we presented a transit light curve of the exoplanet WASP-12b. These data were obtained in 2009 January with the triple-beam camera ULTRACAM mounted on the WHT. We obtained simultaneous light curves in three filters: Sloan u', and two longer wavelength narrow-band filters. The motivation for these observations was to attempt a photometric equivalent of the transmission spectroscopy technique which has been successfully used from both the ground and in space to characterize the atmospheres of transiting exoplanets. At the time of our observation WASP-12b was the hottest known transiting exoplanet, and so an excellent target with which to test this technique.

The main aim of our observations was to measure the planetary radius at three different wavelengths. Properly accounting for the various correlations between system parameters makes a reliable determination a non-trivial task. We have been careful when analysing our data to correctly propagate all potential sources of error throughout our analysis so that the quoted uncertainties on our final radius determinations are a realistic depiction of the limitations of our data. An important part of this is that after we divide our target light curve by the light curves of the comparisons, we do not apply any additional correction to the residual trends in our data. We fit these trends as a component in our model. The reliability of our results is also greatly aided by the fact that our three light curves were obtained and fitted simultaneously. We examine the effect of perturbing some of the parameters in our model, and conclude that while the correlations between the parameters might introduce some systematic bias to our planetary radius measurements, the ratio of the radius determinations in the three wavebands is robust and reliable.

Our data show no evidence for a difference in planetary radius over the wavelength range we study. We calculate the predicted planetary radius difference if the atmosphere were dominated by Rayleigh scattering, as in HD 209458b and HD 189733b. This atmosphere model is consistent with our findings. We also calculate atmosphere models for the two classes of hot Jupiter given in Fortney et al. (2008), which predicts the major opacity sources in the atmosphere are TiO and VO, or Na and K, depending on the planetary temperature. Both of these models are also consistent with our radius measurements. Our radius measurements have an average precision of 2.6 per cent, which is close to the differences which the models predict over this wavelength range (~1.4–2.4 per cent). For planets with a larger atmospheric scale height, measurements with this precision would be effective at distinguishing between the models. Future applications of the transit photometry technique to WASP-12b would benefit from the measurement of multiple transits, as well as the choice of an object with more bright comparison stars in the field of view. Reducing the photon noise contribution from the comparison stars would enable us to obtain more precise determinations of the planetary radius.

We also examined our data for signs of an early ingress at blue wavelengths, which has been reported for this system in the near-UV using *HST* transmission spectra. All three of our light curves show an identical time of ingress and egress.

REFERENCES

Bean J. L., Miller-Ricci Kempton E., Homeier D., 2010, Nat, 468, 669
Bergfors C. et al., 2013, MNRAS, 428, 182
Bisikalo D., Shematovich V., Ionov D., Kaygorodov P., 2012, in COSPAR Meeting, Vol. 39, 3D Gas Dynamic Simulation of the Interaction Between the "Hot Jupiter" Planet and Its Host Star. Abstract E1.4-1-12, p. 196
Charbonneau D., Brown T. M., Noyes R. W., Gilliland R. L., 2002, ApJ, 568, 377
Claret A., 2000, A&A, 363, 1081
Claret A., Bloemen S., 2011, A&A, 529, A75
Copperwheat C. M., Marsh T. R., Dhillon V. S., Littlefair S. P., Hickman R., Gänsicke B. T., Southworth J., 2010, MNRAS, 402, 1824

Cowan N. B., Machalek P., Croll B., Shekhtman L. M., Burrows A., Deming D., Greene T., Hora J. L., 2012, ApJ, 747, 82

Deming D., Seager S., Richardson L. J., Harrington J., 2005, Nat, 434, 740

Dhillon V. S. et al., 2007, MNRAS, 378, 825

Fortney J. J., Lodders K., Marley M. S., Freedman R. S., 2008, ApJ, 678, 1419

Fortney J. J., Shabram M., Showman A. P., Lian Y., Freedman R. S., Marley M. S., Lewis N. K., 2010, ApJ, 709, 1396

Fossati L. et al., 2010, ApJ, 714, L222

Harrington J., Luszcz S., Seager S., Deming D., Richardson L. J., 2007, Nat, 447, 691

Haswell C. A. et al., 2012, ApJ, 760, 79

Hebb L. et al., 2009, ApJ, 693, 1920

Jensen A. G., Redfield S., Endl M., Cochran W. D., Koesterke L., Barman T., 2012, ApJ, 751, 86

Knutson H. A., Charbonneau D., Noyes R. W., Brown T. M., Gilliland R. L., 2007, ApJ, 655, 564

Kurucz R. L., 1979, ApJS, 40, 1

Lai D., Helling C., van den Heuvel E. P. J., 2010, ApJ, 721, 923

Lecavelier des Etangs A., Pont F., Vidal-Madjar A., Sing D., 2008a, A&A, 481, L83

Lecavelier des Etangs A., Vidal-Madjar A., Désert J., Sing D., 2008b, A&A, 485, 865

Lecavelier des Etangs A. et al., 2010, A&A, 514, A72

Llama J., Wood K., Jardine M., Vidotto A. A., Helling C., Fossati L., Haswell C. A., 2011, MNRAS, 416, L41

Maciejewski G. et al., 2013, A&A, 551, A108

Pollacco D. et al., 2008, MNRAS, 385, 1576

Pont F., Knutson H., Gilliland R. L., Moutou C., Charbonneau D., 2008, MNRAS, 385, 109

Redfield S., Endl M., Cochran W. D., Koesterke L., 2008, ApJ, 673, L87

Sing D. K., Vidal-Madjar A., Désert J., Lecavelier des Etangs A., Ballester G., 2008, ApJ, 686, 658

Sing D. K. et al., 2011, MNRAS, 416, 1443

Sing D. K. et al., 2012, MNRAS, 426, 1663

Snellen I. A. G., Albrecht S., de Mooij E. J. W., Le Poole R. S., 2008, A&A, 487, 357

Southworth J., 2008, MNRAS, 386, 1644

Southworth J. et al., 2009, MNRAS, 396, 1023

Southworth J., Mancini L., Maxted P. F. L., Bruni I., Tregloan-Reed J., Barbieri M., Ruocco N., Wheatley P. J., 2012a, MNRAS, 422, 3099

Southworth J. et al., 2012b, MNRAS, 426, 1338

Stevenson K. B., Bean J. L., Seifahrt A., Desert J.-M., Madhusudhan N., Bergmann M., Kreidberg L., Homeier D., 2013, preprint (arXiv:1305.1670)

Swain M. et al., 2013, Icarus, 225, 432

Vidal-Madjar A., Lecavelier des Etangs A., Désert J.-M., Ballester G. E., Ferlet R., Hébrard G., Mayor M., 2003, Nat, 422, 143

Vidal-Madjar A. et al., 2004, ApJ, 604, L69

Zhou G., Bayliss D. D. R., 2012, MNRAS, 426, 2483

This paper has been typeset from a TEX/LATEX file prepared by the author.